



Original Research Paper

Microstructure and microhardness of high entropy alloys with Zn addition: AlCoFeNiZn and AlCoFeNiMoTiZn



M.A. Avila-Rubio^a, C. Carreño-Gallardo^b, J.M. Herrera-Ramirez^b, B.A. García-Grajeda^a,
F.A. Pérez-González^c, J.H. Ramirez-Ramirez^c, N.F. Garza-Montes-de-Oca^{c,*}, F.J. Baldenebro-Lopez^{a,*}

^aFacultad de Ingeniería Mochis, Universidad Autónoma de Sinaloa, Prol. Ángel Flores y Fuente de Poseidón, S.N., 81223 Los Mochis, Sinaloa, México

^bCentro de Investigación en Materiales Avanzados (CIMAV), Laboratorio Nacional de Nanotecnología, Miguel de Cervantes 120, 31136, Chihuahua, Chihuahua, México

^cFacultad de Ingeniería Mecánica y Eléctrica, Universidad Autónoma de Nuevo León, San Nicolás de los Garza, México

ARTICLE INFO

Article history:

Received 23 July 2021

Received in revised form 5 October 2021

Accepted 13 October 2021

Available online 27 October 2021

Keywords:

High entropy alloys

Equiatomic multicomponent alloys

Powder metallurgy

Microstructure

Microhardness

ABSTRACT

High entropy alloys were designed from equiatomic multicomponent systems using powder metallurgy including mechanical alloying and sintering. The structure and morphology of the resulting alloys were characterized by means of X-ray diffraction, scanning electron microscopy, transmission electron microscopy techniques and their hardness values were also determined in the Vickers scale. The results indicate under the milling conditions used, the AlCoFeNiZn, AlCoFeNiMoTi and AlCoFeNiMoTiZn alloys crystallized forming BCC structures whereas the AlCoFeNi alloy presented two different phases, one with FCC structure and the other one with BCC. The synthesis method resulted in alloys with grain sizes in the nano scale having values between 4.1 and 9.4 nm on the powder form up to 40.1 nm after sintering phenomenon which lead to phase transformations which were more evident in the Mo-containing alloys. In addition, the AlCoFeNiZn and AlCoFeNiMoTiZn alloys did not show Zn traces after sintering as it was suggested by chemical analyses using energy dispersive spectroscopy, suggesting it is lost by evaporation during sintering process. Mo-containing systems exhibited the highest microhardness in both milled and sintered conditions.

© 2021 The Society of Powder Technology Japan. Published by Elsevier B.V. and The Society of Powder Technology Japan. All rights reserved.

1. Introduction

Since their appearance in 2004 [1,2], high entropy alloys (HEAs) have attracted great interest in fields of science and technology. They are defined as alloys with multiple major elements in equiatomic proportions or close to it [3]. They possess singularity of forming phases with FCC and/or BCC crystalline structures, as a result of their high configurational entropy [4]. This characteristics provides them with excellent properties such as high mechanical strength, high hardness, good thermal stability as well as outstanding corrosion and wear resistance [5–9], making them promising alloys for a large applications number in different industries such as automotive, marine and aerospace [10,11]. The main properties in HEAs will depend on the elements that comprised them, their stoichiometry and the fabrication route used to produce them [3,4].

During early stages of knowledge on HEAs, their designed and fabrication was based on the use of transition metal elements such as Co, Fe and Ni which are compatible with each other to form the so-called superalloys [12,13]. Co and Ni presence in HEAs promote high compatibility, favoring solid solutions formation with FCC crystalline structures [14,15], due to their high valence electrons concentration [16,17]. HEAs with FCC structures have been reported to have high ductility and toughness, but have reduced mechanical strength compared to HEAs with BCC structures [6,18]. The presence of Fe and Al promote BCC structures formation. Fe acts as a solvent to form solid solutions which have high thermal stability [19]. Other authors have studied the effect of Ti and Mo in the AlCoCrFeNi system. Ti additions to HEAs generally lead the formation of intermetallic compounds, due to its very negative mixing enthalpy with most elements [20,21]. In contrast, additions of Mo addition favors σ phase formation in rich in Mo, Co, Fe systems which considerably improves alloys hardness but reducing ductility and plasticity [22,23]. Regarding the effect of the element Zn, its presence in HEAs has been barely studied due to its low melting and boiling points. HEAs investigations with Zn reveal that it favors BCC structures formation with severe lattice

* Corresponding authors.

E-mail addresses: nelson.garza@gmail.com (N.F. Garza-Montes-de-Oca), francisco.baldenebro@uas.edu.mx (F.J. Baldenebro-Lopez).

distortions and reduced crystal sizes [24,25]. Based on this premise, in this work, the effect of Zn additions on the synthesis of high entropy systems AlCoFeNi, AlCoFeNiZn, AlCoFeNiMoTi and AlCoFeNiMoTiZn is presented through the analysis and discussion of phase formation during mechanical alloying and then sintering. The effect of phase formation on the evolution of the microhardness of the HEAs studied is also presented.

2. Materials and methods

A group of HEAs were synthesized from elemental powders (aluminum, cobalt, iron, nickel, molybdenum, titanium, and zinc) supplied by Alfa Aesar with purity higher than 99.5 % in weight (metal basis). Initially the powders were mixed in equimolar proportions (as it is shown in Table 1). To evaluate the influence of the grinding time on microstructure of the materials produced, they were mechanically alloyed inside a SPEX 8000 M mill for 5, 10 and 15 h. Hardened steel vials of 1.5 in. in diameter and 2.5 in. deep were used. Hardened steel balls were employed as grinding media in a 10:1 ratio with respect to the powders. The total weight of balls was 45 g, 3 balls of 10 mm and 3 balls of 6 mm diameter, with 4.5 g of powder mixture in each milling. A protective atmosphere was generated using argon gas to reduce or totally avoid the oxidation of the powders during milling and methanol was added as a process control agent. After milling the powders were cold compacted in a hydraulic press, applying a 1.0 GPa uniaxial stress for 5 min, to obtain 5 mm diameter disks. The green compacted samples were then encapsulated and vacuum-sealed in quartz tubes to be sintered by placing them in a radiation tube furnace at 1100 °C for 2 h and then at 1200 °C for an additional hour.

The microstructural changes experienced by the alloys were studied by X-ray diffraction (XRD) using a Bruker D8 Advance diffractometer coupled with a $K\alpha$ Cu lamp whose radiation was produced at 40 kV and 30 mA to obtain measurements at a scan rate of 0.01°/min. From the observed peaks, the lattice parameter (a), crystal size (D) by Scherrer's formula, microstrains (ϵ) by Williamson-Hall UDM method, and dislocation density (δ) of the HEAs in its different milling conditions were calculated [26,27], (see Table 2). The morphology of the alloys and their microstructures were observed using a JEOL JSM-7401F scanning electron microscope (SEM) which was operated at different acceleration voltages and working distances to obtain best image quality during inspection. Alternatively, the nanocrystalline nature of the mechanically alloyed powders was evaluated using a JEOL JEM 2200FS + CS transmission electron microscopy (TEM) with different operation parameters to also obtain information on the systems as well as their crystalline structure which was defined by taking of selected area electron diffraction patterns SAED. Finally, the microhardness values of the multicomponent alloys were obtained in Vickers scale using a LM300AT Leco hardness tester

using loads of 50 and 200 g for powders and sintered samples, respectively. The dwell time used during load application was 10 s.

2.1. Thermodynamic and geometric considerations for phases formation in HEAs

Prior to the synthesis of the alloys, the thermodynamic and geometric characteristics that compose HEAs were determined. By this practice, it is possible to predict their crystalline structure and their state namely solid solutions, intermetallic compounds, metallic glasses etc. Based on values obtained for geometrical and thermodynamic parameters as well as phase formation rules as was described by Guo and Liu ($11 \leq \Delta S_{Conf} \leq 19.5$ J/mol K, $-22 \leq \Delta H_{Mix} \leq 7$ kJ/mol, $\delta \leq 8.5$ %) [28], it was predicted that HEAs systems in this work have high probability to form solid solutions as it is shown in Table 3. This is convenient when developing systems with multiple elements as it is indicated by [29].

While adding elements to the alloys, their ΔS_{Conf} values increase because this variable is proportional to the number of elements number that comprises the alloy. The equimolar composition is also of extreme importance because it promotes the generation of greatest entropy having also a considerable influence on the microstructure and properties of each alloy after synthesis [30]. In contrast, the ΔH_{Mix} experiences an important decrease in alloys containing titanium, due to its high negative enthalpy of formation, making it easy to combine, increasing its tendency to form intermetallic compounds and not solid solutions, especially in medium and low entropy systems.

In addition, the Ω parameter relates entropy and enthalpy effects. Values >1.0 indicate that entropy effect prevails over enthalpy effect favoring the formation of solid solutions. The Ω parameter in conjunction with the parameter δ aid for the prediction of alloys with solid solutions when $\Omega \geq 1.1$ and $\delta \leq 6.6$ met [17]. Under these criteria, the alloys in this work will form solid solutions. Titanium causes the δ parameter largest variation, as it is an element with largest atomic radius within alloys. Therefore, given that Ti is an element with a considerably larger size than rest, it does not favor the arrangement atoms in the FCC crystallin structure, being more likely to form BCC ones, as the latter have a lower packaging factor. Therefore, HEAs containing titanium have a higher δ and a predisposition to form BCC structures.

Finally, VEC is a parameter that helps in crystal structure prediction. For $VEC < 6.87$ values, the formation of BCC structures is favored, and FCC for $VEC > 8$, while for values intermediate to these, BCC and FCC structures will coexist [16]. For this study, VEC calculations showed that the AlCoFeNi alloys (system that we will call alloy "A") and AlCoFeNiMoTiZn (A + MoTiZn) will have both BCC and FCC structures, while in AlCoFeNiMoTi (A + MoTi) only BCC will be formed. AlCoFeNiZn (A + Zn) is predisposed to form only FCC structures. The presence of the element zinc promotes high VEC values, which favors the interaction with more ele-

Table 1
Nominal chemical composition of elemental powders.

Sample		Elements						
		Al	Co	Fe	Ni	Mo	Ti	Zn
AlCoFeNi	at. %	25.0	25.0	25.0	25.0			
	Weight (g)	0.6057	1.3230	1.2537	1.3176			
AlCoFeNiZn	at. %	20.0	20.0	20.0	20.0			20.0
	Weight (g)	0.4567	0.9975	0.9452	0.9935			1.1071
AlCoFeNiMoTi	at. %	16.7	16.7	16.7	16.7	16.6	16.6	
	Weight (g)	0.3527	0.7703	0.7300	0.7672	1.2542	0.6256	
AlCoFeNiMoTiZn	at. %	14.3	14.3	14.3	14.3	14.3	14.3	14.2
	Weight (g)	0.2964	0.6473	0.6134	0.6447	1.0539	0.5258	0.7185

Table 2
Mechanical alloyed HEAs micro-structural parameters.

Alloy	Alloying time (hours)	Structure	Lattice (a) nm	Cristal size (D) nm	Microstrain (ϵ) %	Dislocation density (δ) nm ⁻²
			$d/(\frac{h^2 + k^2 + l^2}{\lambda^2})^{1/2}$	$k\lambda/(\beta \cos\theta)$	$\beta/(4 \tan\theta)$	$1/D^2$
A	5	FCC1	0.362	7.4	1.3	0.018
		BCC1	0.288	5.9	1.6	0.029
	10	FCC1	0.362	7.7	1.2	0.017
		BCC1	0.288	5.4	1.7	0.034
	15	FCC1	0.362	8.4	1.1	0.014
		BCC1	0.288	6.4	1.4	0.025
A + Zn	5	BCC1	0.289	4.4	2.1	0.051
	10	BCC1	0.288	6.4	1.4	0.025
	15	BCC1	0.289	4.1	2.3	0.061
A + MoTi	5	BCC2	0.313	9.4	1.1	0.011
	10	BCC2	0.314	7.9	1.3	0.016
	15	BCC2	0.314	8.6	1.2	0.013
A + MoTiZn	5	BCC2	0.314	7.2	1.4	0.019
		BCC3	0.294	5.4	1.7	0.035
	10	BCC2	0.313	8.4	1.2	0.014
		BCC3	0.293	*	*	*
	15	BCC2	0.313	5.9	1.7	0.029
		BCC3	0.293	5.1	1.8	0.039

* It was not possible to calculate based on the observed XRD patterns.
d = interplanar spacing; (h, k, l) = miller index; k = 0.9; λ = 0.15406 nm.

Table 3
HEAs thermodynamic and geometrical parameters.

Alloy	ΔS_{Conf} (J/molK)	ΔH_{Mix} (kJ/mol)	Ω	δ (%)	VEC	Expected phase-formation	Structure
AlCoFeNi	11.53	-13.75	1.31	5.98	7.5	Solid Solution	BCC-FCC
AlCoFeNiZn	13.38	-10.04	1.85	5.47	8.4	Solid Solution	FCC
AlCoFeNiMoTi	14.90	-20.89	1.32	6.50	6.7	Solid Solution	BCC
AlCoFeNiMoTiZn	16.18	-16.33	1.67	6.02	7.4	Solid Solution	BCC-FCC

ments, increasing possibility to bond and forming structures with higher coordination number, in this case FCC structures and not BCC.

It is important to make clear that thermodynamic and geometric criteria are only a guideline for the design of alloys with multiple elements but, changes between trends marked in theory to experimental results could also be possible.

3. Results and discussion

3.1. Characterization of the powders after milling.

Fig. 1 shows diffraction patterns obtained from the alloys after different milling times. Before mechanical alloy. These reflections disappeared progressively as milling time increased. After 5 h, the reflection relative to the elemental powders disappeared completely. Instead, these were replaced by reflections that appeared with lower intensity but with a more pronounced width. This phenomenon indicates that atoms of the elements are introduced into the crystal structure formed during this process. A summary of the changes in microstructural parameters is shown in Table 2. The tendency to form BCC-type solid solutions, reduced crystal sizes (in the nanometer order) and severe lattice distortions are highlighted. This occurs in all HEAs systems due to the constant fracturing and welding processes which are characteristic of mechanical alloying. After 15 h milling, the diffraction patterns no longer show substantial changes in the reflections, nor traces indicating raw elements. The main difference among HEAs were their microstructural characteristics i.e., solid solutions after mechanical alloying resulted with BCC structures with different lattice parameters

depending on the raw elements used. It is worth mentioning that alloy A was the only system with an FCC type solid solution.

In order to identify the effect of the element zinc, alloys A, A + Zn (Fig. 1a) A + MoTi and, A + MoTiZn (Fig. 1b) were grouped. Particularly, alloy A formed 2 phases, which is in agreement with the calculations using the thermodynamic and geometrical theories. The crystallite size of the solid solutions increased as milling time increased. In addition, a significant change in the phase ratio was also observed (Fig. 1a, AlCoFeNi alloy). After 5 h milling, the BCC structure prevails over the FCC one, while for 10 and 15 h the FCC phase was more abundant. The fact that FCC phase was more abundant can be attributed its VEC value (7.5) which is closer to that an alloy with FCC predominance (VEC > 8) rather than to one with BCC structure whose VEC is far below the calculated value (VEC < 6.87).

The addition of zinc to alloy A (A + Zn) resulted in the formation of only one phase with BCC structure and with a 0.289 nm lattice parameter, which is similar to the lattice parameter of pure Fe (0.287 nm). This indicates that residual elements are incorporated into the Fe crystal structure, forming a single solid solution. The alloy that presented the smallest crystallite size (Table 2), indicating that Zn acted as an element that favors the development of iron-type BCC phase and also as a crystallite size reducer. However, according to thermodynamic and geometrical parameters, A + Zn should have formed an FCC structure.

Contrarily, the analysis of the diffraction patterns of the A + MoTi and A + MoTiZn systems shown in Fig. 1b. A + MoTi XRD patterns suggests that molybdenum also favors a greater microstructural refinement and also the formation of BCC Mo-type formation crystalline structures with average 0.313 nm lattice parameter. They also presented higher crystallinity if compared against the other alloys as it is indicated in Table 2. The reason

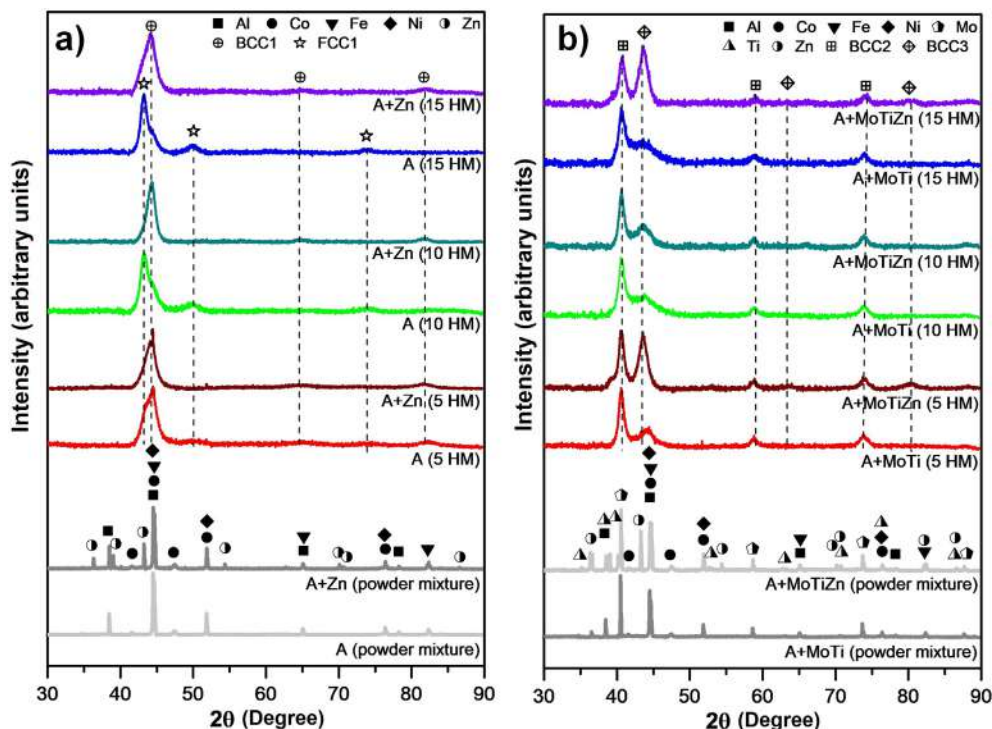


Fig. 1. Diffraction patterns obtained from the alloys after different milling times and before mechanical alloying; (a) AlCoFeNi and AlCoFeNiZn (b) AlCoFeNiMoTi and AlCoFeNiMoTiZn.

by which the BCC Mo structure is predominant is due to several factors. Firstly, Mo is the hardest element and is difficult to deform, therefore, the remaining elements are dissolved in its crystalline structure. Secondly, its large lattice parameter and atomic size facilitate the incorporation of elements into its unit cell over the smaller BCC Fe structure. In contrast, for the A + MoTiZn, Zn addition, generated a second BCC type phase with a 0.293 nm lattice parameter and reflections with displacements at lower angles compared pure Fe. This phenomenon suggests that probably a similar structure is formed, but with greater lattice distortion, due to the considerable number elements that incorporated.

The calculated crystal sizes are summarized in Table 2. Crystallite sizes at nanometer level are common for HEAs obtained by mechanical alloying, due to severe plastic deformations and constant powders fracturing during process. It can be observed that BCC Mo type solid solutions present larger crystal size, up to 9.4 and 8.4 nm for A + MoTi and A + MoTiZn respectively. Contrarily, the A + Zn system exhibited the smallest crystallite sizes in its single-phase BCC Fe structure with 4.1 nm minimum after 15 h milling.

Alternatively, Fig. 2 a to d show the morphological evolution of the precursor powders mixtures. It is possible to identify the different shapes, sizes and textures of elements that comprise them. Where chemical bonding is absent, only physical interaction was present. These characteristics are of great importance as they influence the evolution of the mechanical alloying process. Normally, spherical shapes and smooth surfaces favor cold welding (Al, for example), while irregular shapes and rough surfaces promote fracture (Fe, for example). Both mechanisms occur simultaneously during mechanical alloying triggering a specific microstructure and properties for each HEA [31]. Particularly, Fig. 2 e to h show images of the HEAs powders after 15 h milling. At this point according to the results obtained from XRD, there are no traces of the precursor elements. Therefore, material transfer process was successful one. Undoubtedly, this process promoted the for-

mation of solid solutions in powders that resulted after milling. All alloys presented rough surfaces and irregular shapes, which are distinctive characteristics of powders obtained by mechanical milling. The powder size after milling was main difference between alloys. The analysis of the SEM images indicated that the A + Zn and A + MoTiZn systems included the smallest particle sizes. Therefore, it is possible to state that there direct effect by the addition of Zn to these alloys in particular. In addition, the powders in their final state presented little or no agglomeration, which means that the milling conditions led to an equilibrium between the welding and fracture processes.

The semi-quantitative elemental composition of the alloying system was measured by EDX and the results are summarized in Table 4. From this analysis it is evident that there was no uniform distribution of the elements that comprise the alloys. They were maintained in almost in equimolar conditions, without significant deviations from their initial composition. Elements such as Fe, Co and Ni always exhibited percentages above nominal starting values. This may be due to their high chemical affinity, which facilitates solid solutions formation among them, allowing their signals to prevail. Aluminum was the element which experienced the greatest variation with respect to its initial percentage. This can be attributed to the reason that Al is the element with lowest atomic number, which produces a lower X-ray flux during analysis giving abnormal results. None of the HEAs presented undissolved elements signals, suggesting high element dissolution rates, a mechanism favored by the mechanical alloying process. For other synthesis methods it would be impossible to alloy aluminum and molybdenum due to their different melting points hence the importance of the mechanical alloying effect observed in this work.

In addition, dark-field micrographs obtained by transmission electron microscopy TEM, for a single powder particle of each HEA, are shown in Fig. 3 a to d. From these images, the HEAs nanocrystalline nature could be confirmed after 15 h milling. Moreover, Fig. 3 e to h show the SAED patterns of the powders

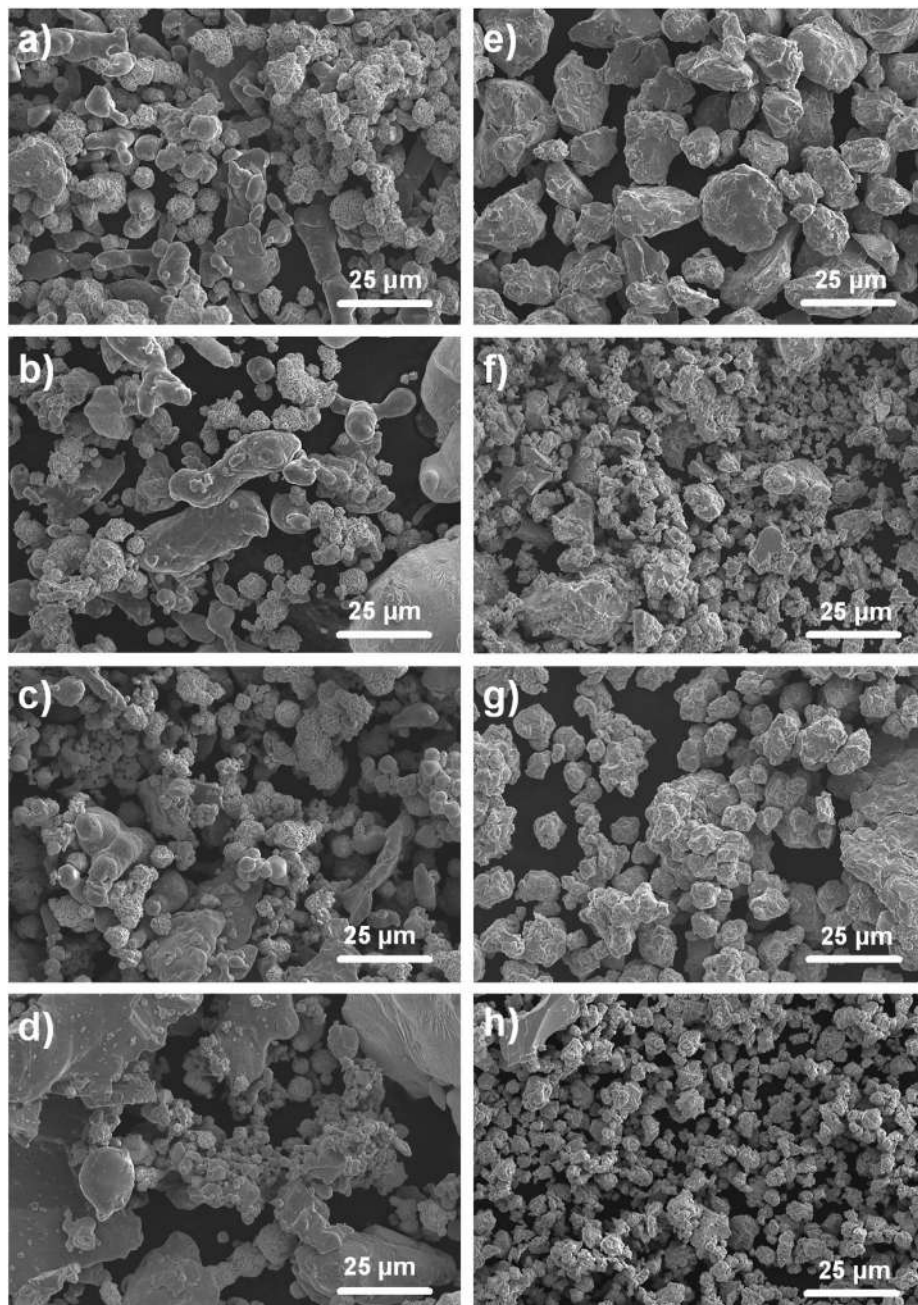


Fig. 2. SEM micrographs of the powder mixtures: (a) AlCoFeNi; (b) AlCoFeNiZn; (c) AlCoFeNiMoTi; (d) AlCoFeNiMoTiZn. SEM micrographs alloyed powders 15 h: (e) AlCoFeNi; (f) AlCoFeNiZn; (g) AlCoFeNiMoTi; (h) AlCoFeNiMoTiZn.

Table 4
Mechanical alloyed HEAs chemical composition (SEM/EDX and TEM/EDS).

Sample		Element at. %						
		Al	Co	Fe	Ni	Mo	Ti	Zn
AlCoFeNi	SEM/EDS	19.2	28.0	28.0	24.8			
	TEM/EDS	26.7	23.6	24.6	25.1			
AlCoFeNiZn	SEM/EDS	15.0	23.8	25.8	21.3			14.1
	TEM/EDS	20.1	27.5	22.0	17.3			13.0
AlCoFeNiMoTi	SEM/EDS	13.7	18.3	19.5	17.9	14.4	16.2	
	TEM/EDS	16.5	16.5	17.4	18.8	17.2	13.6	
AlCoFeNiMoTiZn	SEM/EDS	10.4	16.0	16.4	16.0	11.5	13.9	15.8
	TEM/EDS	5.0	16.1	17.0	15.4	17.5	14.6	14.4

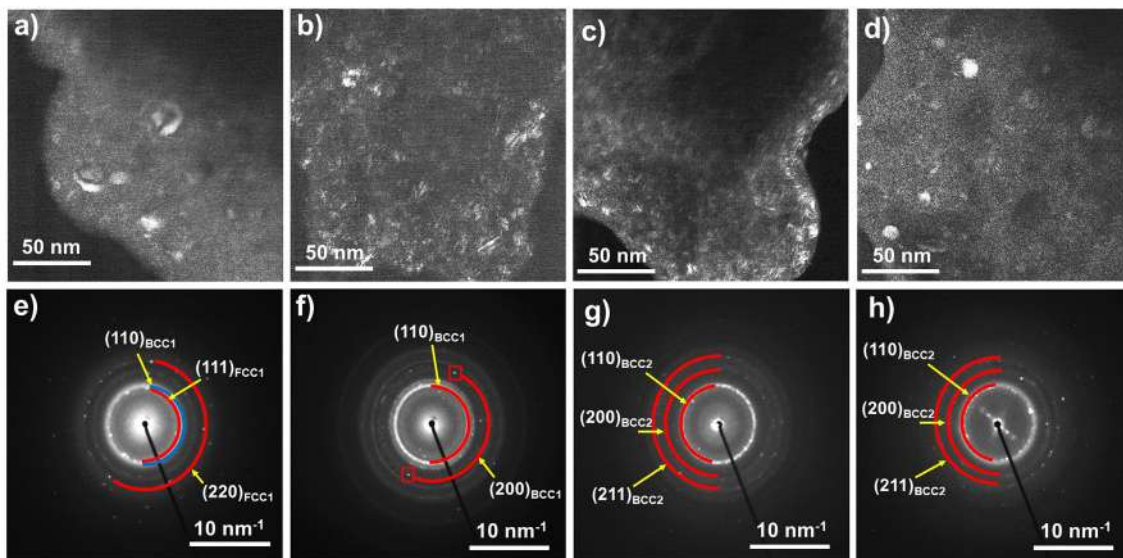


Fig. 3. Dark field TEM images of the alloyed powders 15 h: (a) AlCoFeNi; (b) AlCoFeNiZn; (c) AlCoFeNiMoTi; (d) AlCoFeNiMoTiZn. SAED patterns are: (e) AlCoFeNi; (f) AlCoFeNiZn; (g) AlCoFeNiMoTi; (h) AlCoFeNiMoTiZn.

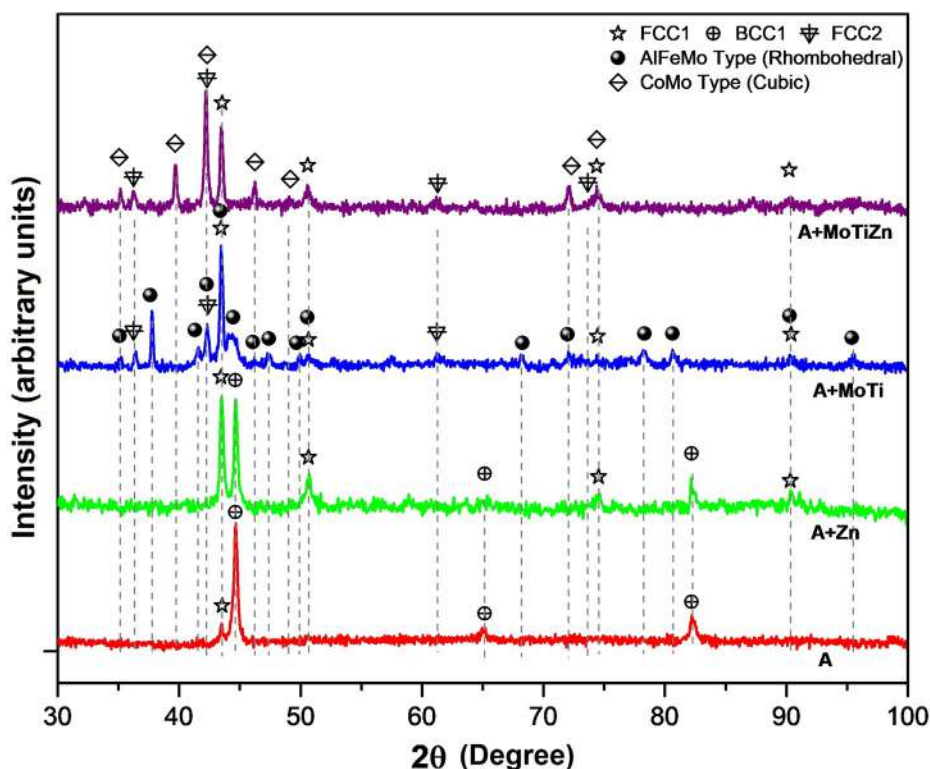


Fig. 4. XRD patterns of sintered HEAs.

of each alloying system. Signals that correspond to the main crystalline structure of each alloy, previously identified in XRD spectra of Fig. 1. Confirm the presence of the BCC crystalline structures for alloys with 5 or more elements as it is shown in (Fig. 3). While for alloy A, an FCC structure prevailed as it is indicated in Fig. 3a. The summary of the TEM/EDX results are presented in Table 4, evidencing the presence of all the elements within the selected area at the time of EDX inspection. It is worth mentioning that alloy A presented the best elemental distribution, with percentages very close

to equimolar while A + Zn exhibited a Zn percentage below nominal and A + MoTiZn a quite low Al content. The remaining elements (Co, Fe, Ni, Mo, Ti) were found in constant percentages according to their initial content.

3.2. Characterization of the sintered alloys.

After sintering, the HEAs were also studied by XRD. The diffraction spectra are shown in Fig. 4. With exception alloy A, all HEAs

Table 5
Crystallite size of the sintered HEAs.

Sample	Crystal structure size (nm)				
	BCC	FCC1	FCC2	AlFeMo Type	CoMo Type
AlCoFeNi	20.8	30.0			
AlCoFeNiZn	19.4	20.2			
AlCoFeNiMoTi		29.6	27.8	41.6	
AlCoFeNiMoTiZn		30.0	26.1		27.7

Table 6
Chemical composition (SEM/EDS) of individual phases of the sintered HEAs.

Sample	Phase	Element at. %						
		Al	Co	Fe	Ni	Mo	Ti	Zn
AlCoFeNi	1	9.5	29.2	42.4	18.9			
	2	32.2	21.2	21.3	25.4			
AlCoFeNiZn	1	20.9	25.5	30.1	23.5			
	2	30.3	20.2	21.6	27.9			
AlCoFeNiMoTi	1	7.1	21.0	26.6	13.3	27.3	4.7	
	2	11.6	19.7	25.0	10.7	28.5	4.5	
	3	24.2	17.5	19.1	30.1	1.9	6.6	
AlCoFeNiMoTiZn	1	12.4	16.0	16.0	11.3	41.7	2.7	
	2	13.8	24.3	31.6	21.6	7.2	1.5	
	3	30.5	18.3	18.8	29.5	1.1	1.8	

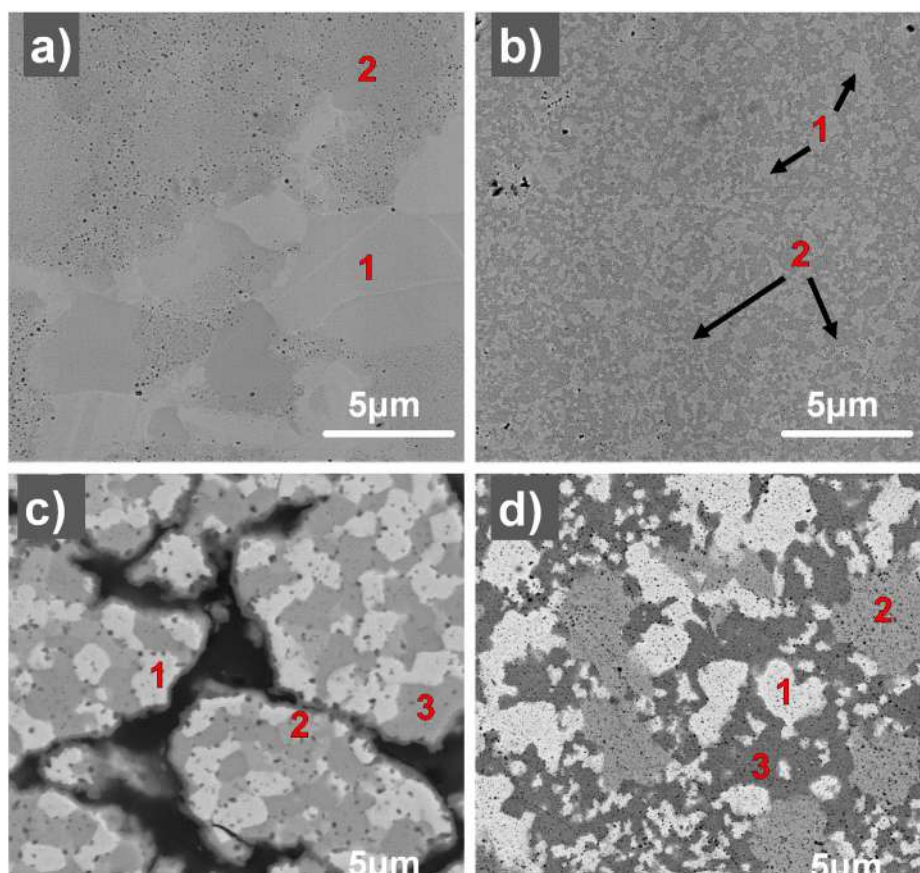


Fig. 5. Backscattered electron SEM micrographs of the sintered HEAs; (a) AlCoFeNi; (b) AlCoFeNiZn; (c) AlCoFeNiMoTi; (d) AlCoFeNiMoTiZn.

exhibited phase transformations after the sintering process. It is observed that only the FCC1 phase is constant in all four alloys, with an estimated 0.360 nm lattice parameter, which is very similar to FeNi binary system identified 00–047–1417 ICDD card. The

phase crystallite size ranged from 20.2 to 30.0 nm depending on each alloy as it is indicated in Table 5.

The alloy A exhibited the same phases as in its powder condition, with difference that after sintering, the BCC1 phase is much more marked and intense. The BCC1 presented 0.286 nm lattice

parameter, which is similar to pure Fe and the crystallite size calculated for this phase within alloy A was 20.8 nm (Table 5).

As it can be seen in Fig. 4, alloys A and A + Zn exhibited similar trends in terms of reflection positions but were different in intensity terms. The system A + Zn went from having a single phase in its powder condition to two phases in its sintered one. The crystallite size of both was very similar, BCC1 = 19.4 nm and FCC1 = 20.2 nm (Table 5) which is indicative of homogeneity in the phase ratio. Both phases lattice parameters agree with those exhibited by the phases of alloy A. However, the width of the peaks in the A + Zn is slightly greater than for alloy A, suggesting greater grain refinement.

Moreover, for the A + MoTi system, the main Mo-type BCC2 phase observed as a powder was replaced by a phase similar to a rhombohedral AlFeMo type, identified with reference code 00–049–1512. This phase included the greatest crystallite size in the four alloys studied, reaching 41.6 nm (Table 5). In addition, two more FCC-type phases were indexed, a FCC1 phase with a 0.360 nm lattice parameter, present in all alloys and a FCC2 phase with 0.428 nm lattice parameter, which only appeared in titanium-containing systems.

In addition, for the alloy with the maximum number of elements, the A + MoTiZn system exhibited three phases after sintering. Like the A + MoTi system, this alloy it contained the FCC1 and FCC2 phases. The main difference was that the A + MoTiZn alloy included reflection with greater intensity of a phase similar to a CoMo type, identified according to ICDD card file number 03–065–7128 and whose presence is associated with a BCC2 Mo structure phase transformation. Finally, the CoMo type structure was main phase the A + MoTiZn in its sintered condition with a crystallite size was 27.7 nm (Table 5).

As it can be seen from diffraction spectra shown in Fig. 4, the principal difference established among the alloys was the number of phases and their distribution. However, although crystallite sizes presented variation depending on the system, they remained within the same order of magnitude and conserved their nanocrystalline nature, Table 5.

The information obtained from the XRD spectra suggest that after sintering, HEAs exhibited remarkable microstructural

changes, which were studied by means of SEM analysis. Energy dispersive X-ray spectroscopy (EDX) was used to evaluate elemental distribution in each phases all alloys. The results of the EDX analyses are summarized in Table 6 and indicate that A + Zn and A + MoTiZn alloys do not show Zn traces. The boiling point of Zn is 907 °C, while the sintering temperatures were 1100 and 1200 °C. It is possible to assume that Zn present in both alloys was lost by evaporation during sintering process [32]. This suggests the Zn weak binding within the solid solutions formed during the mechanical milling. Zn loss in A + Zn and A + MoTiZn alloys makes them equal to A and A + MoTi alloys in terms of element number but, regarding their microstructures, they showed considerable differences.

The backscattered electron micrographs taken with the SEM shown in Fig. 5 give the representative microstructure for the different HEA systems. The A + Zn alloy presented two distinctive zones (Fig. 5b), one present in a light gray tone and with a high Fe concentration, 30.1 at.% which is assumed to be the microstructure of the BCC1 phase. The second zone included a darker tone, and presented Al and Ni contents above their nominal concentration, 30.3 and 27.9 at.%, respectively. As both elements present FCC structures, it is proposed that this phase corresponds to phase identified as FCC1. No Zn content was found in A + Zn, so it presents the same elements as alloy A. However, its phase constitution and microstructure were different. In Fig. 5a and b it is possible to observe how A + Zn exhibits a more refined microstructure with better defined grain boundaries and smaller grain sizes. In addition, A + Zn exhibited a more homogeneous elemental and phase distribution compared to alloy A.

In addition, the backscattered electron micrographs the SEM images shown in Fig. 5c and d, correspond to alloys A + MoTi and A + MoTiZn. Both alloys presented three phases and precipitates in homogeneously distributed black dots form. The main difference being established for the alloy A + MoTi alloy which had a high pore content. Bright gray phase present in the A + MoTiZn alloy (marked as 1 in the micrograph) is rich in Mo (41.7 at.%), which possibly came from the BCC2 phase which was observed for the alloy in its milling condition. Alternatively, the zone marked as 2 is rich in Fe (31.6 at.%) and it would correspond to FCC2 struc-

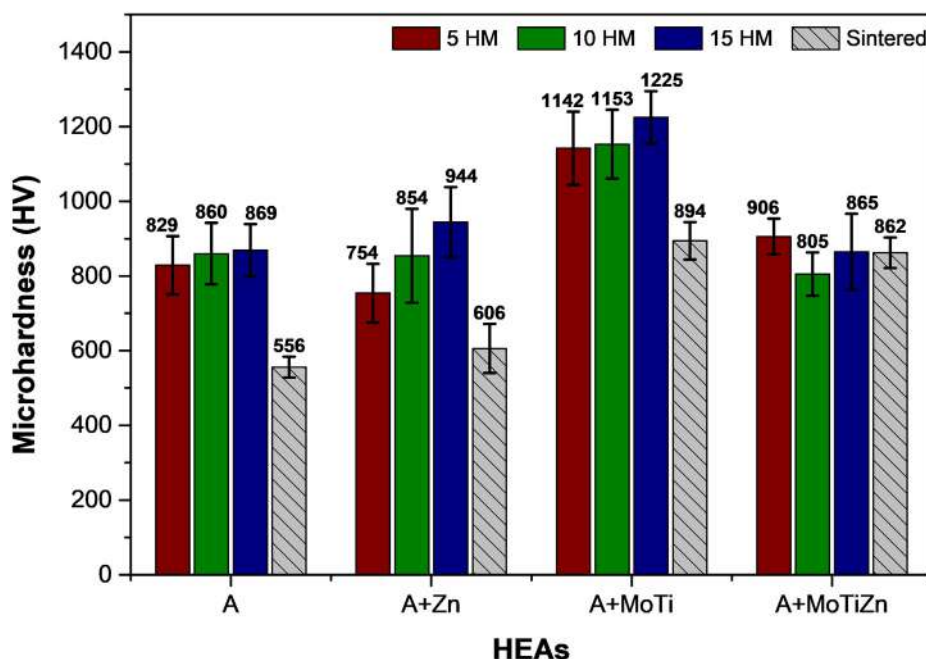


Fig. 6. Microhardness results of HEAs studied.

ture. Finally, the dark gray color zone marked as 3 in the micrographs, can be associated with the FCC1 structure that appeared in all alloys, being rich in Al (30.5 at.%) and Ni (29.5 at.%) respectively. It is important to mention that precipitates were formed during sintering at high temperature and its presence can be regarded as TiC as it has been mentioned in similar investigations of HEAs which were fabricated with elements similar to those used in this work [33,34].

Finally, for the A + Zn and A + MoTiZn alloys, the Zn loss during sintering favored the refinement of the grain size. Based on the results obtained, it is possible to suggest the use of a low boiling point elements in HEAs synthesis, to obtain a better control of the microstructure of the alloys, once this experiences sublimation during high temperature sintering.

3.3. Microhardness tests

Fig. 6 shows the microhardness values of the alloys in Vickers scale for different milling conditions after sintering. The HEAs exhibited high hardness and high dependence on the elements that composed them. The HEAs fabricated by the powder metallurgy route, favoured the formation of microcrystalline and even nanocrystalline structures with high hardness. With A + MoTiZn exception, all alloys increased in hardness with increasing milling time. A + MoTi was significantly harder than the rest alloys, with 1225 HV_{0.05}. It's possible to observe that from 5 to 10 h milling there was a decrease in hardness in A + MoTiZn. This coincides with phase amorphization identified as BCC3, which can be seen in diffraction patterns in Fig. 1b, and which undoubtedly affected the performance of the alloy during testing.

After sintering, all HEAs showed a decrease in hardness. This behavior was expected, because high sintering temperatures dissolve the micro deformations obtained during mechanical milling by erasing the cold work exerted during this fabrication route. The comparison between alloy A and A + Zn allows to state that there was an increment in hardness although when sintered, they presented the same phases. However, the difference in the microhardness values is because the A + Zn system includes a more refined microstructure with smaller crystallite size, which resulted in a greater hardness. In addition, the alloys containing molybdenum were the ones that reached highest hardness values during testing. Despite its high porosity, the A + MoTi alloy was the hardest of sintered samples, reaching 894 HV_{0.20}. In spite of the all the processing routes experienced by the alloying systems here studied, the high hardness values obtained for all systems can be best attributed to the formation of solid solutions (caused by high entropy of mixing) and to strain hardening which is the principal hardening mechanisms for alloys fabricated by this route.

4. Conclusions

- 1) In this study, it was found that for the reported alloys with five or more elements the BCC-type microstructures prevail in their milled condition which include homogeneous elements distribution without particle agglomeration evidence.
- 2) All HEAs fabricated exhibited nanometric structures that were preserved even after the sintering process. The A + Zn and A + MoTiZn alloying systems exhibited zinc loss due to elevated sintering temperature. However, this fact favored their microstructural refinement compared to equivalent A and A + MoTi systems.
- 3) FCC1 phase with average 0.360 nm lattice parameter, was only one that remained constant in all alloys in their sintered condition. Molybdenum-containing alloys reached

highest hardness values, both in milled and post-sintering condition.

Declaration of Competing Interest

The authors declare that they have no known competing financial interests or personal relationships that could have appeared to influence the work reported in this paper.

Acknowledgments

M.A. Avila-Rubio was supported as a graduate student by CONACYT (grant 701859). The authors would also like to thank Universidad Autónoma de Sinaloa, Universidad Autónoma de Nuevo León, Centro de Investigaciones en Materiales Avanzados SC and Laboratorio Nacional de Nanotecnología (NanoTech) for the facilities provided to develop this work.

References

- [1] J.W. Yeh, S.K. Chen, S.J. Lin, J.Y. Gan, T.S. Chin, T.T. Shun, C.H. Tsau, S.Y. Chang, Nanostructured high-entropy alloys with multiple principal elements: novel alloy design concepts and outcomes, *Adv. Eng. Mat.* 6 (2004) 299–303, <https://doi.org/10.1002/adem.200300567>.
- [2] B. Cantor, I.T.H. Chang, P. Knight, A.J.B. Vincent, Microstructural development in equiatomic multicomponent alloys, *Mat. Sci. Eng. A* 375–377 (2004) 213–218, <https://doi.org/10.1016/j.msea.2003.10.257>.
- [3] B.S. Murty, J.W. Yeh, S. Ranganathan, *High-entropy alloys, first ed.*, B.H. London, 2014.
- [4] M.C. Gao, J.W. Yeh, P.K. Liaw, Y. Zang, *High-Entropy Alloys: Fundamentals and Applications, first ed.*, Springer, Switzerland, 2016.
- [5] T.M. Butler, J.P. Alfano, R.L. Martens, M.L. Weaver, High-Temperature Oxidation Behavior of Al-Co-Cr-Ni-(Fe or Si) Multicomponent High-Entropy Alloys, *Jom* 67 (2015) 246–259, <https://doi.org/10.1007/s11837-014-1185-7>.
- [6] Z. Li, K.G. Pradeep, Y. Deng, D. Raabe, C.C. Tasan, Metastable high-entropy dual-phase alloys overcome the strength-ductility trade-off, *Nature* 534 (2016) 227–230, <https://doi.org/10.1038/nature17981>.
- [7] M. Yang, X.J. Liu, H.H. Ruan, Y. Wu, H. Wang, Z.P. Lu, High thermal stability and sluggish crystallization kinetics of high-entropy bulk metallic glasses, *J. Appl. Phys.* 119 (2016), <https://doi.org/10.1063/1.4955060> 245112.
- [8] J.H. Zhao, X.L. Ji, Y.P. Shan, Y. Fu, Z. Yao, On the microstructure and erosion-corrosion resistance of AlCrFeCoNiCu high-entropy alloy via annealing treatment, *Mater. Sci. Technol. (United Kingdom)* 32 (2016) 1271–1275, <https://doi.org/10.1080/02670836.2015.1116494>.
- [9] B. Gludovatz, A. Hohenwarter, D. Catoor, E.H. Chang, E.P. George, R.O. Ritchie, A fracture-resistant high-entropy alloy for cryogenic applications, *Science* 345 (2014) 1153–1158, <https://doi.org/10.1126/science.1254581>.
- [10] J.W. Yeh, Y.L. Chen, S.J. Lin, S.K. Chen, High-Entropy Alloys – A New Era of Exploitation, *Mater. Sci. Forum* 560 (2007) 1–9, <https://doi.org/10.4028/www.scientific.net/MSF.560.1>.
- [11] S. Praveen, H.S. Kim, High-Entropy Alloys: Potential Candidates for High-Temperature Applications – An Overview, *Adv. Eng. Mater.* 20 (2018) 1–22, <https://doi.org/10.1002/adem.201700645>.
- [12] J.M. Torralba, P. Alvarado, A. García-Junceda, High-entropy alloys fabricated via powder metallurgy, A critical review, *Powder Metall.* 62 (2019) 84–114, <https://doi.org/10.1080/00325899.2019.1584454>.
- [13] M. Vaidya, G.M. Muralikrishna, B.S. Murty, High-entropy alloys by mechanical alloying: A review, *J. Mater. Res.* 34 (2019) 664–686, <https://doi.org/10.1557/jmr.2019.37>.
- [14] Y. Zhang, T.T. Zuo, Z. Tang, M.C. Gao, K.A. Dahmen, P.K. Liaw, Z.P. Lu, Microstructures and properties of high-entropy alloys, *Prog. Mater. Sci.* 61 (2014) 1–93, <https://doi.org/10.1016/j.pmatsci.2013.10.001>.
- [15] M. Vaidya, A. Prasad, A. Parakh, B.S. Murty, Influence of sequence of elemental addition on phase evolution in nanocrystalline AlCoCrFeNi: Novel approach to alloy synthesis using mechanical alloying, *Mater. Des.* 126 (2017) 37–46, <https://doi.org/10.1016/j.matdes.2017.04.027>.
- [16] S. Guo, C. Ng, J. Lu, C.T. Liu, Effect of valence electron concentration on stability of fcc or bcc phase in high entropy alloys, *J. Appl. Phys.* 109 (2011), <https://doi.org/10.1063/1.3587228> 103505.
- [17] X. Yang, Y. Zhang, Prediction of high-entropy stabilized solid-solution in multi-component alloys, *Mater. Chem. Phys.* 132 (2012) 233–238, <https://doi.org/10.1016/j.matchemphys.2011.11.021>.
- [18] A. Gali, E.P. George, Tensile properties of high- and medium-entropy alloys, *Intermetallics* 39 (2013) 74–78, <https://doi.org/10.1016/j.intermet.2013.03.018>.
- [19] R. M. Pohan, B. Gwalani, J. Lee, T. Alam, J.Y. Hwang, H. J. Ryu, R. Banerjee, S. H. Hong, Microstructures and mechanical properties of mechanically alloyed and

- spark plasma sintered Al_{0.3}CoCrFeMnNi high entropy alloy, *Mater. Chem. Phys.*, 210 (2018) 62–70, <http://doi.org/10.1016/j.matchemphys.2017.09.013>.
- [20] M.H. Tsai, K.Y. Tsai, C.W. Tsai, C. Lee, C.C. Juan, J.W. Yeh, Criterion for sigma phase formation in Cr- and V-Containing high-entropy alloys, *Mater. Res. Lett.* 1 (2013) 207–212, <https://doi.org/10.1080/21663831.2013.831382>.
- [21] M.H. Chuang, M.H. Tsai, W.R. Wang, S.J. Lin, J.W. Yeh, Microstructure and wear behavior of Al_xCo_{1.5}CrFeNi_{1.5}Ti_y high-entropy alloys, *Acta Mater.* 59 (2011) 6308–6317, <https://doi.org/10.1016/j.actamat.2011.06.041>.
- [22] T.T. Shun, L.Y. Chang, M.H. Shiu, Microstructure and mechanical properties of multiprincipal component CoCrFeNiMo_x alloys, *Mater. Charact.* 70 (2012) 63–67, <https://doi.org/10.1016/j.matchar.2012.05.005>.
- [23] C.C. Juan, C.Y. Hsu, C.W. Tsai, W.R. Wang, T.S. Sheu, J.W. Yeh, S.K. Chen, On microstructure and mechanical performance of AlCoCrFeMo_{0.5}Ni_x high-entropy alloys, *Intermetallics* 32 (2013) 401–407, <https://doi.org/10.1016/j.intermet.2012.09.008>.
- [24] M. Murali, S.P.K. Babu, B.J. Krishna, A. Vallimanan, Synthesis and characterization of AlCoCrCuFeZn_x high-entropy alloy by mechanical alloying, *Prog. Nat. Sci. Mater. Int.* 26 (2016) 380–384, <https://doi.org/10.1016/j.pnsc.2016.06.008>.
- [25] S. Varalakshmi, M. Kamaraj, B.S. Murty, Processing and properties of nanocrystalline CuNiCoZnAlTi high entropy alloys by mechanical alloying, *Mater. Sci. Eng. A* 527 (2010) 1027–1030, <https://doi.org/10.1016/j.msea.2009.09.019>.
- [26] R. Sivakami, S. Dhanuskodi, and R. Karvembu, Estimation of lattice strain in nanocrystalline RuO₂ by Williamson-Hall and size-strain plot methods, *Spectrochim. Acta - Part A Mol. Biomol. Spectrosc.*, 152 (2016) 43–50, <http://doi.org/10.1016/j.saa.2015.07.008>.
- [27] P. Bindu, S. Thomas, Estimation of lattice strain in ZnO nanoparticles: X-ray peak profile analysis, *J. Theor. Appl. Phys.* 8 (2014) 123–134, <https://doi.org/10.1007/s40094-014-0141-9>.
- [28] S. Guo, C.T. Liu, Phase stability in high entropy alloys: Formation of solid-solution phase or amorphous phase, *Prog. Nat. Sci. Mater. Int.* 21 (2011) 433–446, [https://doi.org/10.1016/s1002-0071\(12\)60080-x](https://doi.org/10.1016/s1002-0071(12)60080-x).
- [29] C.Y. Cheng, Y.C. Yang, Y.Z. Zhong, Y.Y. Chen, T. Hsu, J.W. Yeh, Physical metallurgy of concentrated solid solutions from low-entropy to high-entropy alloys, *Curr. Opin. Solid State Mater. Sci.* 21 (2017) 299–311, <https://doi.org/10.1016/j.cossms.2017.09.002>.
- [30] Y. Zhang, Y.J. Zhou, J.P. Lin, G.L. Chen, P.K. Liaw, Solid-solution phase formation rules for multi-component alloys, *Adv. Eng. Mater.* 10 (2008) 534–538, <https://doi.org/10.1002/adem.200700240>.
- [31] C.D. Gómez, F.J. Baldenebro, C.R. Santillán, I. Estrada, J.A. Matutes, J.M. Herrera, R. Martínez, Microstructural and magnetic behavior of an equiatomic NiCoAlFe alloy prepared by mechanical alloying, *J. Alloys Compd.* 615 (2015) S317–S323, <https://doi.org/10.1016/j.jallcom.2014.01.233>.
- [32] J.F.Q. Rodrigues, G.S. Padilha, A.D. Bortolozzo, W.R. Osório, Effect of sintering time on corrosion behavior of an Ag/Al/Nb/Ti/Zn alloy system, *J. Alloys Compd.* 834 (2020), <https://doi.org/10.1016/j.jallcom.2020.155039> 155039.
- [33] R. Anand Sekhar, S. Samal, N. Nayan, and S. R. Bakshi, Microstructure and mechanical properties of Ti-Al-Ni-Co-Fe based high entropy alloys prepared by powder metallurgy route, *J. Alloys Compd.*, 787 (2019) 123–132, [10.1016/j.jallcom.2019.02.083](https://doi.org/10.1016/j.jallcom.2019.02.083).
- [34] R. Anand Sekhar, S.R. Bakshi, Microstructural Evolution of Ti-Al-Ni (Cr Co, Fe)-Based High-Entropy Alloys Processed Through Mechanical Alloying, *Trans. Indian Inst. Met.* 72 (2019) 1427–1430, <https://doi.org/10.1007/s12666-019-01596-1>.